

---

This is an electronic reprint of the original article.  
This reprint may differ from the original in pagination and typographic detail.

Heise, Katja; Jonkergouw, Christopher; Anaya-Plaza, Eduardo; Guccini, Valentina; Pääkkönen, Timo; Linder, Markus B.; Kontturi, Eero; Kostiainen, Mauri A.

## Electrolyte-Controlled Permeability in Nanocellulose-Stabilized Emulsions

*Published in:*  
Advanced Materials Interfaces

*DOI:*  
[10.1002/admi.202200943](https://doi.org/10.1002/admi.202200943)

Published: 13/09/2022

*Document Version*  
Publisher's PDF, also known as Version of record

*Published under the following license:*  
CC BY-NC-ND

*Please cite the original version:*  
Heise, K., Jonkergouw, C., Anaya-Plaza, E., Guccini, V., Pääkkönen, T., Linder, M. B., Kontturi, E., & Kostiainen, M. A. (2022). Electrolyte-Controlled Permeability in Nanocellulose-Stabilized Emulsions. *Advanced Materials Interfaces*, 9(26), Article 2200943. <https://doi.org/10.1002/admi.202200943>

---

This material is protected by copyright and other intellectual property rights, and duplication or sale of all or part of any of the repository collections is not permitted, except that material may be duplicated by you for your research use or educational purposes in electronic or print form. You must obtain permission for any other use. Electronic or print copies may not be offered, whether for sale or otherwise to anyone who is not an authorised user.

# Electrolyte-Controlled Permeability in Nanocellulose-Stabilized Emulsions

Katja Heise,\* Christopher Jonkergouw, Eduardo Anaya-Plaza, Valentina Guccini, Timo Pääkkönen, Markus B. Linder, Eero Kontturi, and Mauri A. Kostiainen

Particle-stabilized emulsions, so-called Pickering emulsions (PEs), are a promising low-tech avenue to precisely engineered materials for applications in drug delivery, catalysis, or water remediation. The particle assembly at the liquid–liquid interface provides superior stability and an adjustable permeability, which is a key parameter for controllable compound capture and release. However, understanding the complex factors that control the particle assembly in detail is a still-remaining challenge limiting practical applications of PEs in an industrial framework. In this study, the properties of oil-in-water emulsions, stabilized by cellulose nanocrystals (CNCs), are investigated. It is shown how high ionic strength leads to low polydispersity droplets, with restricted permeability across the oil-water interface due to the dense packing of the CNC layer. In contrast, lower electrolyte concentration enables enhanced uptake through the interface, while providing the required stability for the reusability of the material. The authors continue to study the impact of the electrolyte content on the dynamic responses of the emulsions, leading to a liquid–liquid system with tunable cyclic uptake and release levels. Overall, the results highlight the potential of nanocellulose-stabilized emulsions as tunable and robust material platform with well-defined permeability characteristics—made in a simple way.

The micro- or nanoparticles that assemble to the oil–water interface make the difference here. They provide stability to the biphasic environment, stimuli-responsiveness, and structural controllability at the micrometer- and nanometer-scale.<sup>[13–15]</sup>

Adjustable permeability is one key feature of PEs qualifying them for applications in drug or nutrient delivery,<sup>[16]</sup> as reaction environment,<sup>[13]</sup> or water remediation from organic pollutants.<sup>[17,18]</sup> Important factors that influence the permeability are the porosity the particles create at the interface as well as the affinity of, for example, the encapsulated compound to the particle shell defining specific and non-specific interactions. Whereas the porosity has been described to depend on the size, shape and number of particles covering the interface,<sup>[19,20]</sup> affinity characteristics correspond to the surface chemistry of the material.<sup>[21]</sup> Additionally, the ability to release cargo under pre-determined stimuli is a key feature in, for example, drug delivery systems<sup>[22]</sup>

or, if several uptake–release cycles are successfully achieved, a reusable and sustainable removal of contaminants from waste water. Therefore, PEs show an enormous potential to contribute to the United Nations Sustainable Development Goal #6 – Clean Water and Sanitation.

Important design parameters that control the formation, stability and properties of PEs are: 1) the water phase conditions, including pH and ionic strength; 2) the oil phase conditions, particularly, the oil polarity; 3) the oil–water ratio; 4) the amount, aspect ratio, surface chemistry, and roughness of the (nano)particles; and 5) the emulsification process (e.g., sonication versus microfluidic techniques).<sup>[23–26]</sup> Hence, understanding these parameters and the mechanisms behind the particle assembly at liquid–liquid interfaces in detail, unfolds the full potential of PEs as material platform and ultimately facilitates commercial applications.

Biopolymer nanoparticles, like the rod-shaped cellulose nanocrystals (CNCs), are well-established, effective emulsion stabilizers, which has been addressed in a wide range of recent reviews.<sup>[23–25,27,28]</sup> CNCs are isolated top-down from plants or bacterial cellulose. Their surface chemistry is a result of the isolation approach—typically, acid hydrolysis—introducing, for example, negative charges ( $-\text{OSO}_3^-$  or  $-\text{COO}^-$ ) to the

## 1. Introduction

Particle-stabilized emulsions, known as Pickering emulsions (PEs), are a fascinating and versatile platform for functional materials: from the synthesis of Janus particles,<sup>[1–3]</sup> over colloidosomes that compartmentalize incompatible reactants<sup>[4,5]</sup> or function as a reaction environment for cascade reactions,<sup>[6–8]</sup> to PE-based functional foams<sup>[9,10]</sup> and biphasic gels.<sup>[11,12]</sup>

K. Heise, C. Jonkergouw, E. Anaya-Plaza, V. Guccini, T. Pääkkönen, M. B. Linder, E. Kontturi, M. A. Kostiainen  
Department of Bioproducts and Biosystems  
Aalto University  
P.O. Box 16300, Aalto, Espoo FI-00076, Finland  
E-mail: katja.heise@aalto.fi

 The ORCID identification number(s) for the author(s) of this article can be found under <https://doi.org/10.1002/admi.202200943>.

© 2022 The Authors. Advanced Materials Interfaces published by Wiley-VCH GmbH. This is an open access article under the terms of the Creative Commons Attribution-NonCommercial-NoDerivs License, which permits use and distribution in any medium, provided the original work is properly cited, the use is non-commercial and no modifications or adaptations are made.

DOI: 10.1002/admi.202200943

nanocrystal surface.<sup>[29]</sup> As a result of their inherent hydrophilicity, CNCs form oil-in-water (o/w) emulsions.<sup>[30]</sup> Alterations of the surface chemistry, for instance, by hydrophobization, can increase the emulsion stability,<sup>[31]</sup> or enable inverse water-in-oil (w/o) PEs<sup>[32]</sup> and even double o/w/o emulsions.<sup>[33]</sup>

Charged groups (e.g.,  $-\text{OSO}_3^-$  or  $-\text{COO}^-$ ) on the CNC surface and the charge density per se affect the emulsion stability and the structure and porosity of the CNC layer at the interface, where electric repulsion between the anionic CNCs can lead to a destabilization of the emulsion.<sup>[30,34]</sup> On the other hand, the formation of uniform monolayers at the o/w interface is facilitated by the surface charge of the nanocrystals and their colloidal properties in aqueous dispersion.<sup>[30,35,36]</sup> Lowering the surface charge density enhances the stabilization of the CNCs at the o/w interface,<sup>[34]</sup> but can also lead to larger CNC aggregates and emulsions with non-even interfacial layers.<sup>[30]</sup>

The addition of NaCl is a reliable way to screen the negative charges on the CNC surface, which improves the emulsion stability.<sup>[37,38]</sup> Above the critical concentration range, where charge screening and the CNC colloidal stability in water are in balance, NaCl increasingly causes the formation of large, yet stable nanocrystal aggregates.<sup>[39,40]</sup> In biphasic systems, the electrolyte content directly affects the adsorption of CNCs to oil–water and air–water interfaces and the interfacial properties.<sup>[35,36]</sup> Studies on flat, non-emulsified o/w systems have shown that the presence of NaCl in the water phase enhances the adsorption kinetics of anionic CNCs to the interface by increasing the surface pressure.<sup>[35,36]</sup> The addition of NaCl further increased the interface load with CNCs and the viscoelastic properties of the interfacial layer.

In the emulsified state, that is, after high-shear emulsification, the exact effect of the electrolyte content on the interfacial CNC assembly is not yet well understood and, especially, the translation of this effect to specific material properties like permeability characteristics. This study therefore targets to understand how the electrolyte content can be systematically used to control the formation and tune the permeability of o/w PEs, which were stabilized by C6-carboxylated ( $-\text{COO}^-$ ) CNCs. We monitor this tunability by laser-light diffraction and a combined setup of fluorescence spectroscopy, fluorescence microscopy, and time-resolved experiments using the Nile red (NR) dye as model compound. The solvatochromic properties of NR enable permeation across the o/w interface to be monitored, which gives in-depth information on the interfacial properties, as well as the uptake capacity. With this experimental setup we will show that the electrolyte content is an important design parameter when transferring PEs into material applications. Ultimately, it's the understanding of, and control over, the rather simplistic formation of biopolymer-stabilized emulsions that facilitate their use as a versatile material platform.

## 2. Results and Discussion

Oil-in-water PEs (40:60, v/v) were prepared with 0.50 wt% carboxylated CNCs (see Figure S1a, Supporting Information) in the bulk water phase. Dodecane was used as oil phase, which is a very common choice for this type of fundamental, proof-of-concept studies. However, we would expect a significant impact

of the oil phase and, especially, its polarity on the stability and properties of the formed PE droplets.<sup>[36]</sup> The CNCs were obtained from bacterial cellulose (BC) by HCl-gas hydrolysis followed by an oxidative treatment with (2,2,6,6-tetramethylpiperidin-1-yl)oxyl (TEMPO) and NaOCl<sup>[41]</sup> to a degree of polymerization (see Section S2a, Supporting Information) of 291 and a relatively low carboxylate content of  $0.378 \pm 0.011$  mmol  $-\text{COO}^-/\text{g}$  BC. Disintegration of the hydrolyzed and oxidized fibers was achieved by high-pressure microfluidization. The obtained nanocrystals formed stable aqueous dispersions (zeta potential  $[\zeta]: -31.7$  mV, pH 7.3) and had a comparably large crystal length distribution of  $168 \pm 129$  nm (see Figure S1b, Supporting Information).

The impact of the electrolyte content on the emulsion droplet formation (Figure 1) was systematically investigated in a NaCl concentration [NaCl] range from 0 to 100 mM. Salt-free emulsions were stable when freshly prepared. Within 24 h, however, macroscopic phase separation was observed, which was also evident from the large droplet size distribution determined by laser-light diffraction (Figure 1b and Table S1, Supporting Information). The stability of the emulsion system increased notably at a low [NaCl] of 10 mM. Increasing salt concentrations from 10 to 100 mM, decreased the median droplet sizes ( $d_{50}$ ) and the droplet size distribution reached a plateau. This is likely associated with the aspect ratio of the CNCs and their possible maximum load at the interface. Concomitantly to the increasing water phase density at higher [NaCl],<sup>[42]</sup> creaming increased significantly (Figure 1a) forming a dense and clustered layer of small, homogeneous PE droplets, which appeared to be aggregated at 100 mM NaCl. Similar observations were also made by Liu et al.<sup>[43]</sup>

Emulsion stability and droplet size distribution follow a very clear trend: the increased stability of the emulsions and the high number of small droplets may be associated with the screening of the anionic CNC surface charges upon NaCl addition and an enhancement of the surface pressure, as described in the literature.<sup>[44]</sup> These effects, together with the high shear forces during mixing, likely resulted in a fast adsorption of the charged CNCs to the o/w interface and a fast and homogeneous dispersion of the oil droplets in the water phase. This interpretation is in line with studies where the adsorption of anionic CNCs, bearing  $-\text{OSO}_3^-$  groups, to air–water and oil–water interfaces has been measured as a function of the surface pressure at increasing NaCl concentration.<sup>[35,36]</sup> Therefore, we expect that our results for carboxylated CNCs can be translated to other negatively charged CNCs and that the impact of the electrolyte concentration would correspond to the CNC surface charge density.<sup>[30,34]</sup> Moreover, as it was described by Kalashnikova et al., the droplet diameter is inversely proportional to the amount of CNCs available for the interface stabilization.<sup>[20]</sup> Hence, the more CNCs adsorb to the o/w interface at the increasing [NaCl], the smaller the droplets get; and this has been clearly shown for our PEs.

### 2.1. Fluorescence Spectroscopy

Fluorescence spectroscopy was used to elucidate the effects of NaCl on the assembly of the TEMPO-CNCs to the o/w interface and, moreover, on the possible control of the droplet

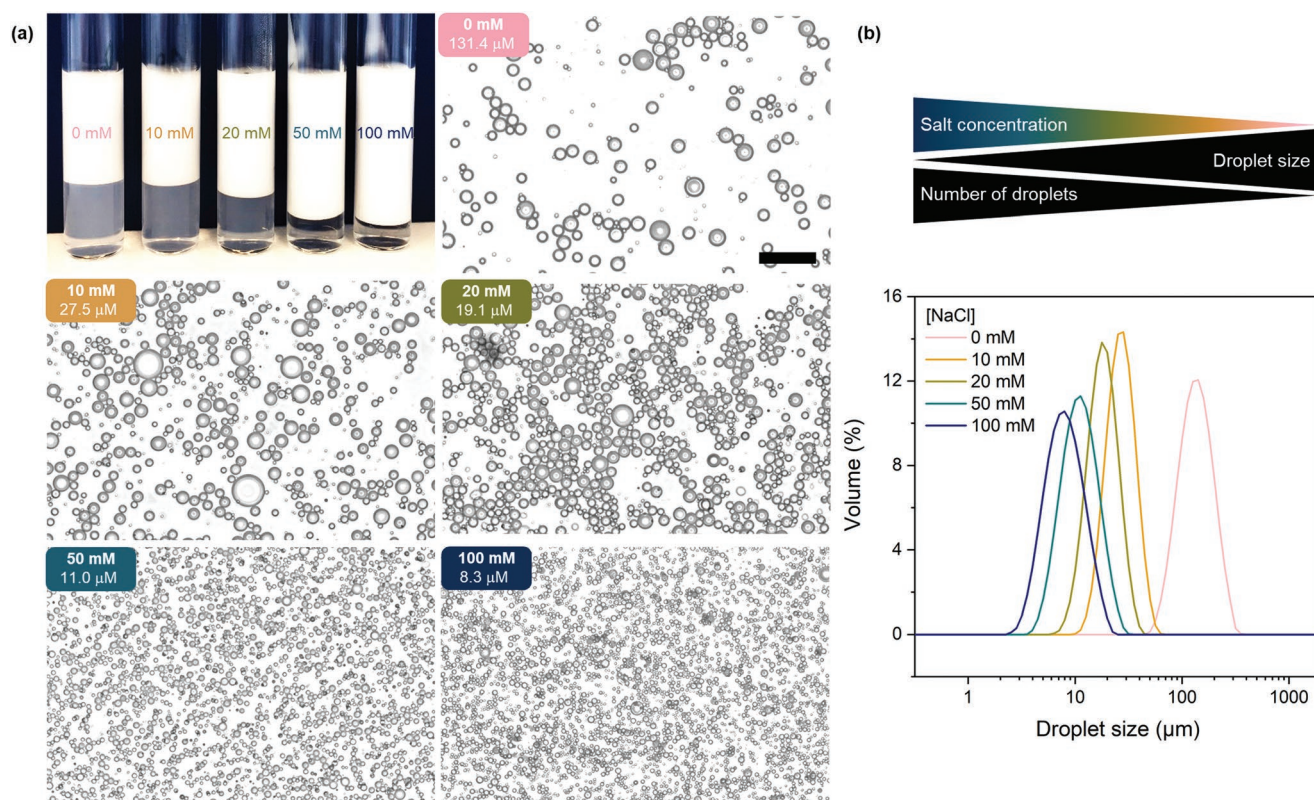


**Figure 1.** Dodecane-in-water (40:60, v/v) emulsions stabilized with 0.50 wt% TEMPO-oxidized CNCs: a) photographs and microscopic contrast images (10 $\times$  magnification, scale bar in all images: 100  $\mu\text{m}$ ) of emulsions with increasing molarity of NaCl in the water phase and the resulting median ( $d_{50}$ ) droplet sizes. All PEs were diluted 1:2 (v/v) with DI water or NaCl solution for the image acquisition. b) Average droplet size distribution measured by laser-light diffraction.

permeability. Nile red (NR) was used as a model compound. This dye has solvent-dependent (solvatochromic) optical properties. Excited at a fixed wavelength of 535 nm, NR has its emission maximum at 635 nm when bound to the CNCs in water suspensions, whereas when dissolved in dodecane, the emission maximum shifts to 570 nm (see Figure S2, Supporting Information). Consequently, permeation of NR across the interface into the droplet core (Figure 2a–c) causes a significant shift in the dye’s fluorescence emission spectrum and delivers valuable information on the interface properties. In water, NR is poorly soluble and shows a highly quenched fluorescent signal centered at ca. 660 nm.

For the spectroscopic analysis (Figure 2d,e), the PEs ([NaCl]: 0–100 mM) were equilibrated with NR at 50 nM for 1 h. This low dye concentration does enable the investigation of the initial distribution of the dye in different PEs, below a possible saturation of the o/w interface and the dodecane core.

The dye partitioning after equilibration is, according to the fluorescence emission spectra (Figure 2d), clearly affected by the salt content. For higher salt concentrations (20, 50, and 100 mM), the dye mainly accumulated at the droplet interfaces ( $\lambda_{\text{em}} = 630 \text{ nm}$ ), associated with the CNCs. At 10 mM NaCl, NR is distributed between the dodecane phase ( $\lambda_{\text{em}} = 570 \text{ nm}$ ) and the interface, resulting in two distinct emission maxima. In salt-free emulsions, the strongest detectable fluorescent signal originates from a dye dissolved in dodecane. Single-point analysis at 570 and 630 nm (Figure 2e) provides more

precise, semi-quantitative information on the dye partitioning in the different PE systems, which follows a very clear trend: the fluorescence emission at 630 nm (i.e., NR at o/w interface) increases significantly with the salt concentration, whereas the fluorescence emission at 570 nm (i.e., NR at dodecane phase) declines. Overall, this trend suggests a restricted permeability of the CNC interface layer at high [NaCl]. This could either originate from a reduced porosity, or from stronger interactions between NR and the CNCs at the interface. Both explanations would suggest a higher number of nanocrystals and denser packing of the interfacial CNC layer<sup>[36]</sup> (Figure 2c) at high electrolyte contents. The impact of porosity on the permeation of a small molecule like NR is less likely, since we expect nanopores even in densely packed CNC layers.

Another important observation is the high fluctuation of the 570 nm signal in the PEs with 0 and 10 mM NaCl. This might further correspond to the lower stability of those emulsions—hence, free dodecane due to a starting phase separation or an insufficient emulsification. This issue is further explored below.

To investigate how the dye partitioning is affected by an increasing availability of NR, we carried out a titration experiment, varying the ratio between NR-to-PE droplets. The NR concentration was kept constant at 5  $\mu\text{M}$  to avoid concentration-related effects, and PEs with 10, 20 and 50 mM NaCl, for which we expected the most significant changes, were diluted with salt solution (see Tables S2 and S3, Supporting Information). The decrease of PE available, correlated to the CNC concentration

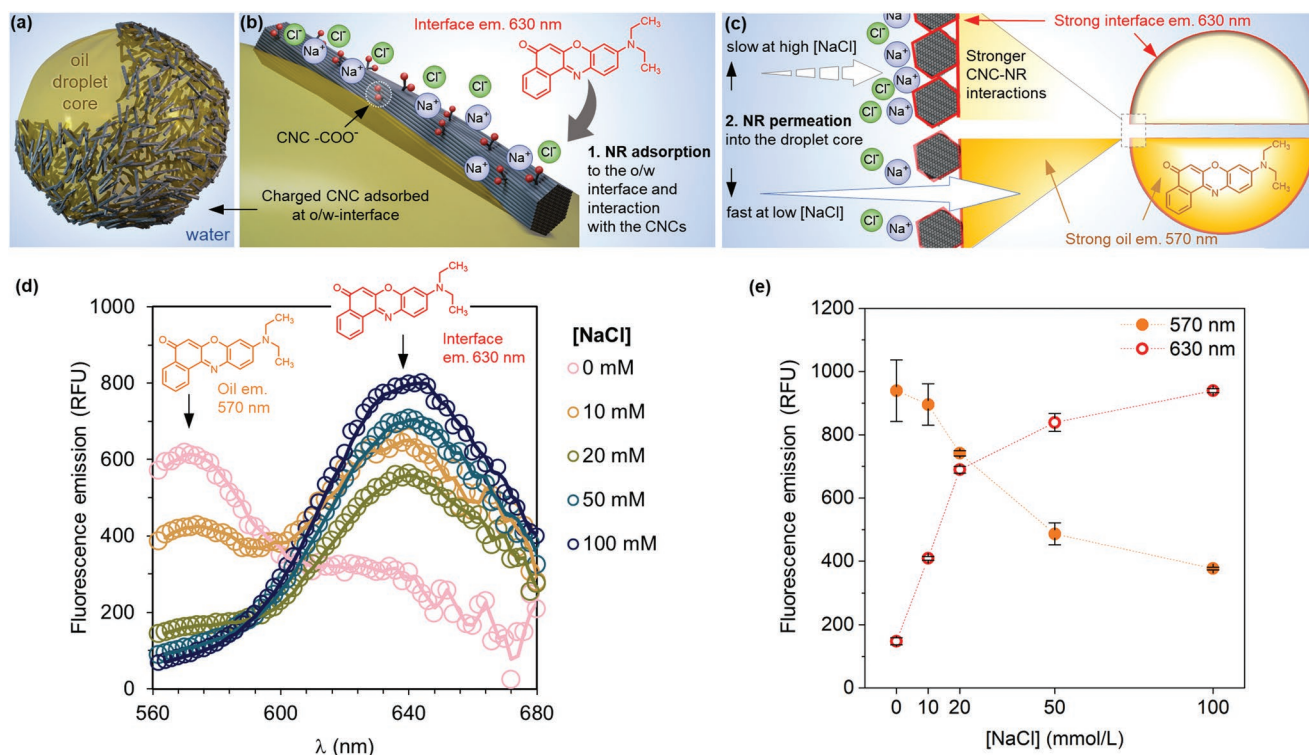


**Figure 2.** a–c) Schematic illustration of a) a CNC-stabilized emulsion droplet and b,c) the solvatochromic experiments in PEs showing the effect of the salt concentration on the partitioning of NR. b) NR adsorbs to the o/w interface and interacts with the CNCs ( $\lambda_{em} = 630$  nm) assembled there. c) At high electrolyte contents, densification of the CNC layer at the o/w interface leads to enhanced CNC-NR interactions and a slower permeation of the dye into the droplet core. At low [NaCl], the dye permeation across the interface is more favorable resulting in a stronger fluorescence signal from the oil phase ( $\lambda_{em} = 570$  nm). d) Fluorescence spectra (empty circles: measured, average data [ $n = 3$ ]); line: added trend line) and e) single-point-analysis (average values [ $n = 3$ ], error bars: standard deviation) reveal how the [NaCl] affected the dye partitioning between interface and droplet core in PEs equilibrated with a low NR charge (50 nm).

(in nanomoles per milligram), is effectively increasing the NR-to-PE ratio (Figure 3).

In the initial, undiluted emulsions, the fluorescence emission spectra (Figure 3a) show the same trend as observed before (Figure 2d) for the low NR concentration: the 570 nm signal (dodecane phase) decreases significantly with the increasing salt concentration. When increasing the dye-to-PE ratio (i.e., effectively increasing the NR concentration), the dye started to permeate into the droplets of all three PEs, albeit to a different extent depending on the salt concentration. Figure 3b shows the single-point-analysis at 570 and 630 nm. Accordingly, the 630 nm signal follows the same trend for all three PEs and reaches similar emission values, whereas the oil-core emission is significantly lower for the 50 mM PE. At 50 mM NaCl, the uptake (marked with a sharp increase in signal) occurs at higher NR/CNC ratios and the oil-core fluorescence reaches just a fraction of the emission value of the 10 or 20 mM NaCl PEs. Hence, NR needs to be in a higher ratio to the PEs to promote the crossing of the o/w interface. These observations are schematically summarized in Figure 3c.

The behavior of NR itself is counterintuitive, as this hydrophobic dye would theoretically migrate more efficiently to the oil phase at increasing ionic strengths in the bulk water. This, combined with the observed partitioning of the dye, is another indication for the restricted permeability of the droplet interface due to denser CNC packing and enhanced CNC-NR interactions at high NaCl concentrations. However, for a further elucidation

and interpretation of these interactions, fluorescence spectroscopy has several clear limitations. First, it is impossible to distinguish between the dodecane phase encapsulated by CNCs and free dodecane outside the emulsion droplets. The same applies to free, dispersed CNCs in the bulk water phase or CNCs assembled at the interface. Moreover, the decrease of the fluorescence emission from the oil-core at increasing salt concentrations might simply coincide with the decreasing droplet sizes, improving the distribution of dye at the CNC interface layer. For instance, the surface-area-to-volume ratio (see Table S1, Supporting Information), calculated from the median ( $d_{50}$ ) droplet sizes, increases from 0.05 (0 mM NaCl) to 0.72 (100 mM NaCl) and, thus, the available droplet surface area for the dye adsorption. It has been also shown that the fluorescence of NR quenches when the dye molecules aggregate in confined space, which might explain the lower fluorescence emission in the smaller droplets at high [NaCl].<sup>[45]</sup> Particularly, the role of the particle size on the dye partitioning will be addressed in the following microscopy section showing that the ratio between interface to oil core fluorescence is size-independent.

## 2.2. Fluorescence Microscopy

Getting around the limitations of spectroscopy, fluorescence microscopy was used as a complementary method to observe the behavior of single, immobilized droplets. The different

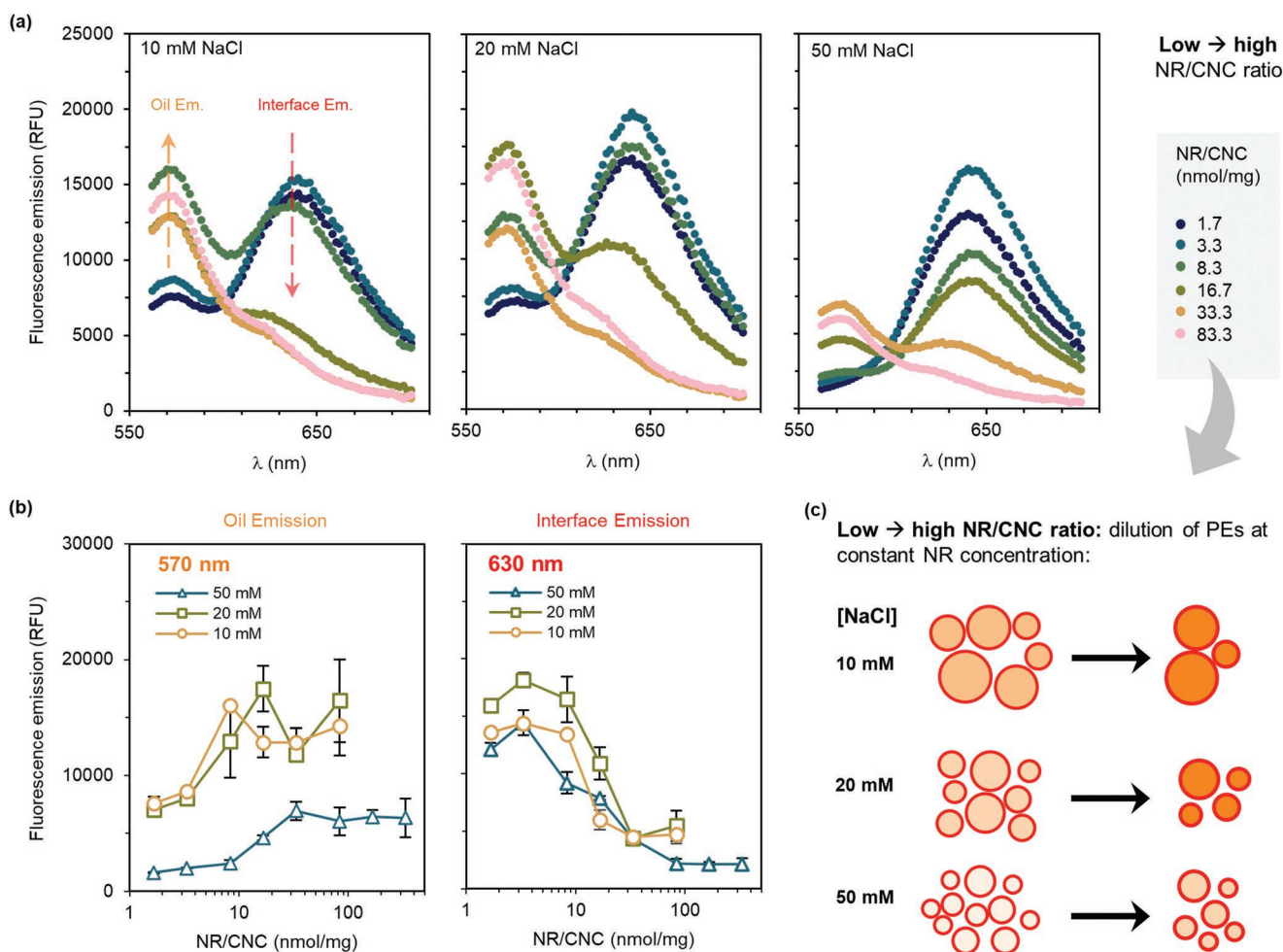


**Figure 3.** Titration of a constant concentration of NR (5  $\mu\text{M}$ ) with decreasing amount of PE (given in milligrams CNC). The development of the average ( $n = 3$ ) fluorescence spectra (a) and the average ( $n = 3$ ) single-point fluorescence at 570 and 630 nm (b), with respect to the salt content ([NaCl]: 10, 20 or 50 mM), shows that with increasing NR/CNC ratio, more NR is present in the dodecane core for all three salt concentrations. However, as schematically illustrated in (c), whereas the adsorption of NR to the interface occurs to the same extent for all [NaCl], the permeation of NR into the oil-core decreases significantly at 50 mM NaCl.

PEs ([NaCl]: 0–100 mM) were equilibrated with NR at 10  $\mu\text{M}$  for 1 h, giving a sufficient fluorescence signal, and the droplets were immobilized on polyethylenimine (PEI)-coated microscopy slides. With this, potentially free, non-encapsulated oil phase could be washed off. A combined setup with two different fluorescence filters enabled a separate observation of the fluorescence signal from the interface ( $\lambda_{\text{ex}} = 528\text{--}550$  nm,  $\lambda_{\text{em}} = 615\text{--}675$  nm), appearing as a smooth, homogeneous layer, and the signal from the dodecane core ( $\lambda_{\text{ex}} = 528\text{--}550$  nm,  $\lambda_{\text{em}} = 560\text{--}584$  nm) filling the entire droplet area (Figure 4a). Additionally, a counterstaining of the droplets with Calcofluor white (CFW,  $\lambda_{\text{ex}} = 418\text{--}442$  nm,  $\lambda_{\text{em}} = 461\text{--}485$  nm) selectively stained the CNCs as a control for specific localization at the interface. Besides, the CFW stain clearly revealed the presence of a significant amount of free CNCs in the bulk water phase of the 10 mM NaCl PE which, hence, were not adsorbed to the o/w interface (see Figure S3 and Section S5b, Supporting Information). At the droplet focus point, however, these non-adsorbed CNCs were not detectable and did not interfere with the image acquisition.

The CFW staining was observable as hollow shells, and comparable to the appearance of NR residing at the o/w interface. However, compared to CFW, NR seems to form a very even layer at the interface. This can be simply explained by the different specific and non-specific interactions of the two dyes with the CNCs and their solubility in the water and oil phase, which determines interactions with the o/w interface. Due to its lipophilic nature, NR distributes between o/w interface and the dodecane core, where it preferably accumulates.<sup>[46]</sup> Hence, the dye very likely interacts non-specifically with the CNCs from both the water and the oil side of the interface. In contrast, CFW is known to very specifically bind to the OH-groups of polysaccharides<sup>[47]</sup> which are, according to the current prevailing model,<sup>[30]</sup> immersed in the water phase. However, the resolution threshold limits further insights of the interface morphology.

3D reconstructions (Figure 4b; Movies S1 and S2, Supporting Information) illustrate even more clearly the partitioning of NR in the different chemical environments. CFW and NR at the interface appear as hollow spheres, while the NR fluorescence

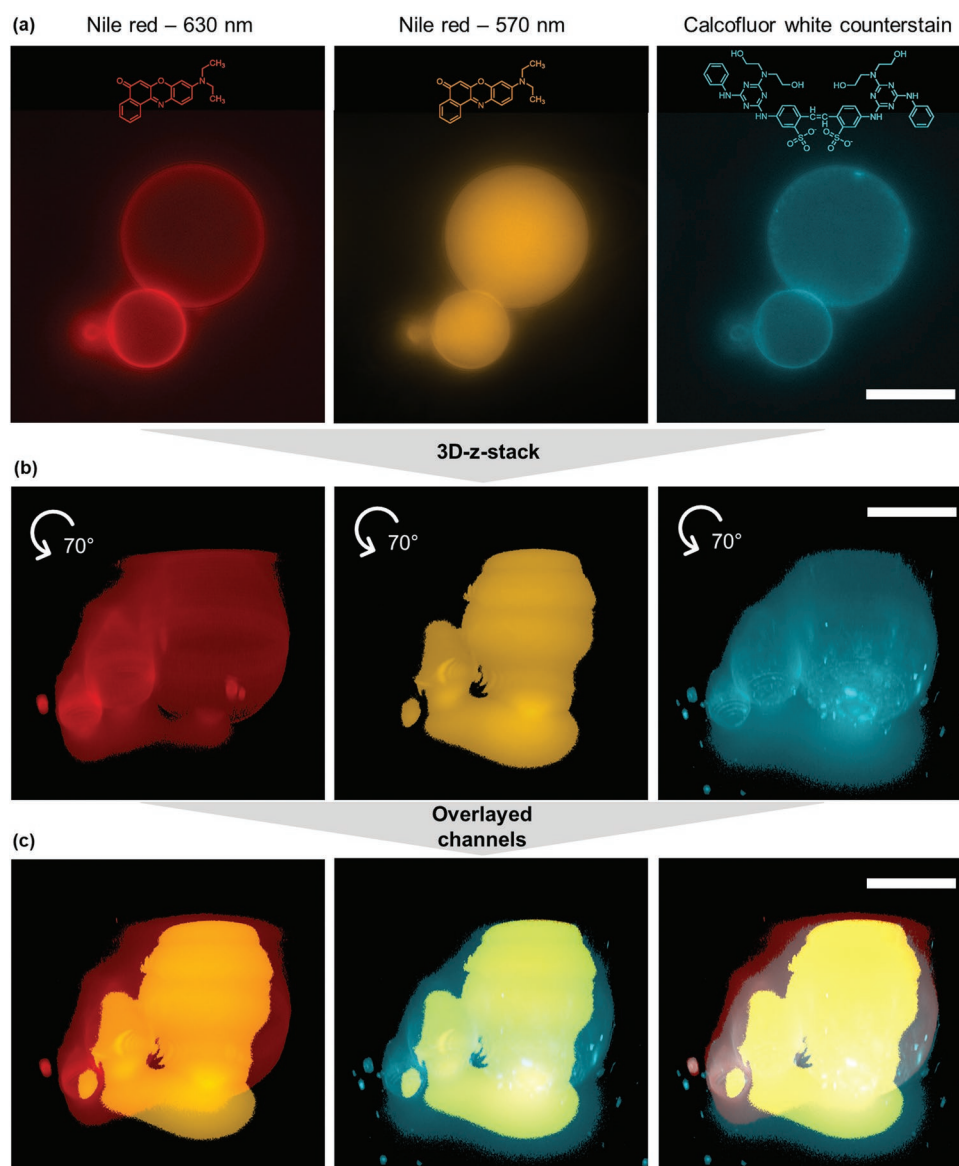


**Figure 4.** Counterstaining of the PE droplets (10 mM NaCl, immobilized on PEI-coated glass slides) with calcofluor white (CFW, right, chemical structure shown) and NR (left and middle, 10  $\mu$ M) for fluorescence microscopy (zoom-in, 100 $\times$  magnification, scale bar in all images: 20  $\mu$ m): a) while CFW only stains the CNCs at the o/w interface with high selectivity, NR distributes between the o/w interface and the droplet core. 3D z-stack reconstructions (70° viewing angle) (b) and overlays (c) of the different channels clearly show the difference between the smooth interface, the CNC interfacial layer, and the filled oil droplet core.

from the dodecane phase emerges as solid, filled droplets. Overlaying the different channels (Figure 4c) further highlights the different locations of the dyes. This counterstaining experiment, thus, confirms and increases our understanding of the localization of the solvatochromic dye.

Equilibration of the different PEs ([NaCl]: 0–100 mM) with NR (10  $\mu$ M) resulted in a very different appearance of the droplets in the red (630 nm), orange (570 nm) (Figure S4, Supporting Information), and merged red/orange channel (Figure 5a). From each channel, a fluorescence profile can be extracted for single, selected particles (Figure 5b), which were very distinct for the different salt concentrations. Moreover, the extracted core-to-interface (570-to-630 nm) relative fluorescence units

(RFU) ratio can provide essential information on the dye partitioning with respect to the [NaCl] (Figure 5c), similar to fluorescence spectroscopy for the emulsion bulk (see Figure 3b). Here, the RFU ratio was measured over the whole droplet area for 50 selected droplets in a diameter range between ca. 3–55  $\mu$ m. With this, fluorescence microscopy provides a direct correlation between dye distribution and droplet size. Over the measured droplet size range, the partitioning of the dye between core-to-interface is size-independent. This is a key result and essential information that was missing from fluorescence spectroscopy. The RFU ratio remains constant despite the particle diameter but decreases linearly from 0 to 50 mM NaCl. Hence, this behavior is solely an effect of the salt concentration, which

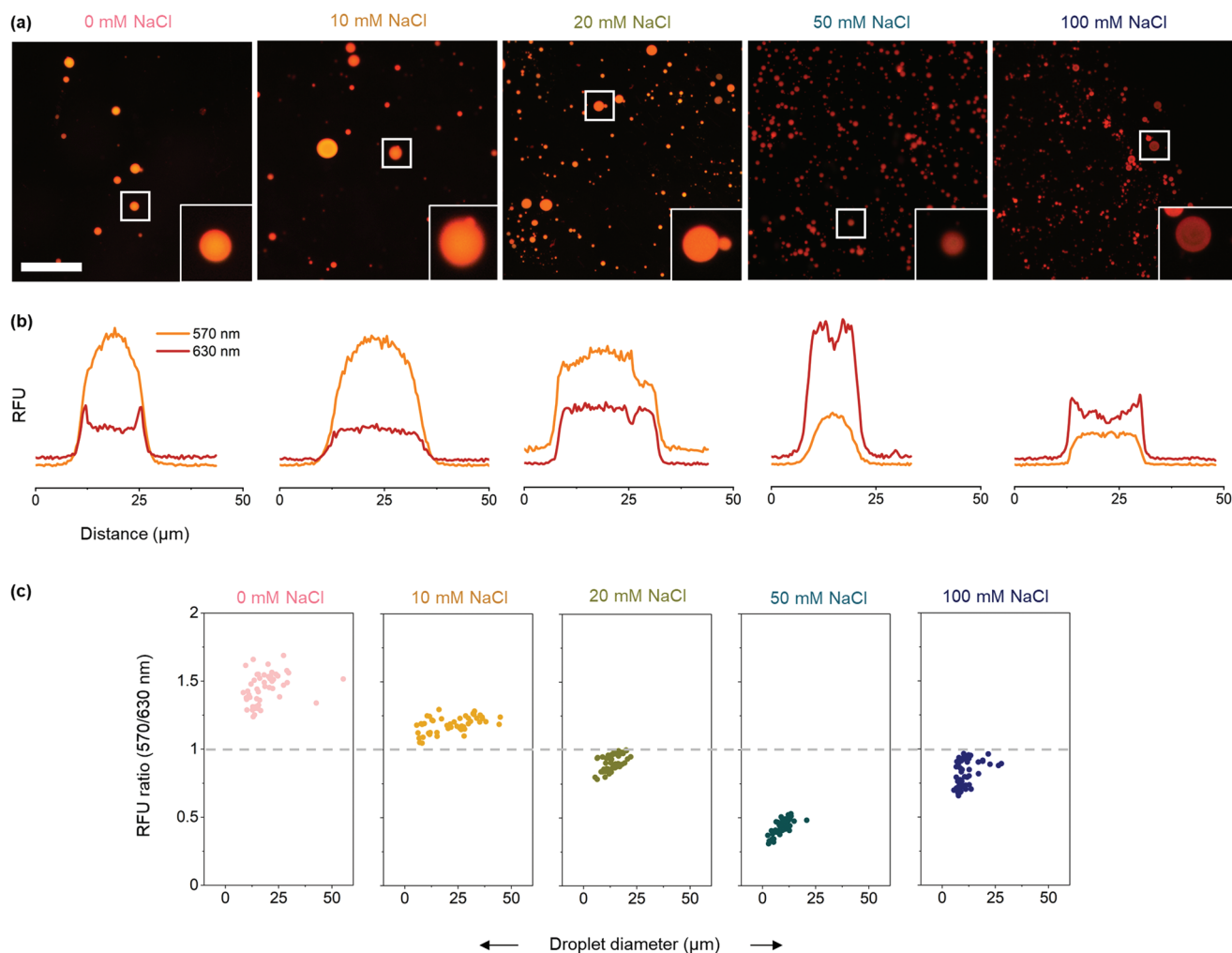


**Figure 5.** Fluorescence microscopy with PEs equilibrated with 10  $\mu\text{M}$  NR: a) micrographs (20 $\times$  magnification, scale bar: 100  $\mu\text{m}$ ) showing the merged orange (oil-core emission, 570 nm) and red (interface emission, 630 nm) fluorescence channel for the different PEs ([NaCl]: 0–100 mM). The RFU profiles in (b) correspond to the zoom-ins of the highlighted droplets in (a) and their 570 and 630-nm fluorescence signal, recorded over the emulsion droplet cross section. The RFU ratios (oil-core versus interface) in (c) were calculated for 50 selected droplets (single data points shown) for each NaCl concentration and with respect to the droplet size. This proves that the dye distribution between core and interface is size-independent.

again suggests differences in the interface properties associated with the CNC layer density. We can also exclude our aforementioned speculation that the dye distribution coincides with the increasing surface-area-to-volume ratio.

Surprisingly, for the highest salt concentration of 100 mM NaCl, the RFU 570/630 ratio increases again, indicating the higher presence of dye in the droplet core when compared to [NaCl] = 50 mM. This observation might be explained by an increased, uncontrolled aggregation of the CNCs at 100 mM NaCl since the formation of a smooth nanocrystal monolayer at the interface is based on a sensitive interplay between surface charge screening and colloidal stability.<sup>[30,40]</sup> This aggregation could increase the porosity of the interfacial CNC layer leading to a faster NR permeation, while decreasing the available CNC surface area for the CNC-dye interactions.

### 2.3. Time-Resolved Nile Red Uptake

To further investigate the impact of the NaCl concentration on the dye interface adsorption and core permeation rate, we

carried out time-resolved, dynamic experiments. This allowed stepwise droplet loading with NR. The applied dynamic flow led to the detachment of the PE droplets from the PEI-coated glass slides. For this reason, we switched to poly-L-lysine for the immobilization, which provided superior attachment of PE droplets to the glass surface. Microscopy images (Figure 6a) were acquired every 2 min, for a total of three different areas on the glass slide, acquiring both the red (630 nm filter) and orange (570 nm filter) intensities. After the droplets were sufficiently immobilized and before the addition of NR, the droplets were stained with CFW (55  $\mu\text{M}$ ). This counterstaining served as a stability factor during the experiment, as it enabled the monitoring of potential changes in the CNC layer. After staining the droplets with CFW, NR was loaded to the system by increasing the concentration stepwise from 1 to 5  $\mu\text{M}$ . Any potential effects of the CFW counterstain on the later NR uptake of the PE droplets, was excluded by measuring the 570/630 nm RFU ratios of particles stained with both dyes (see Figure S5, Supporting Information), as compared to our approach in Figure 5c. This shows that the extracted ratios for counterstained droplets

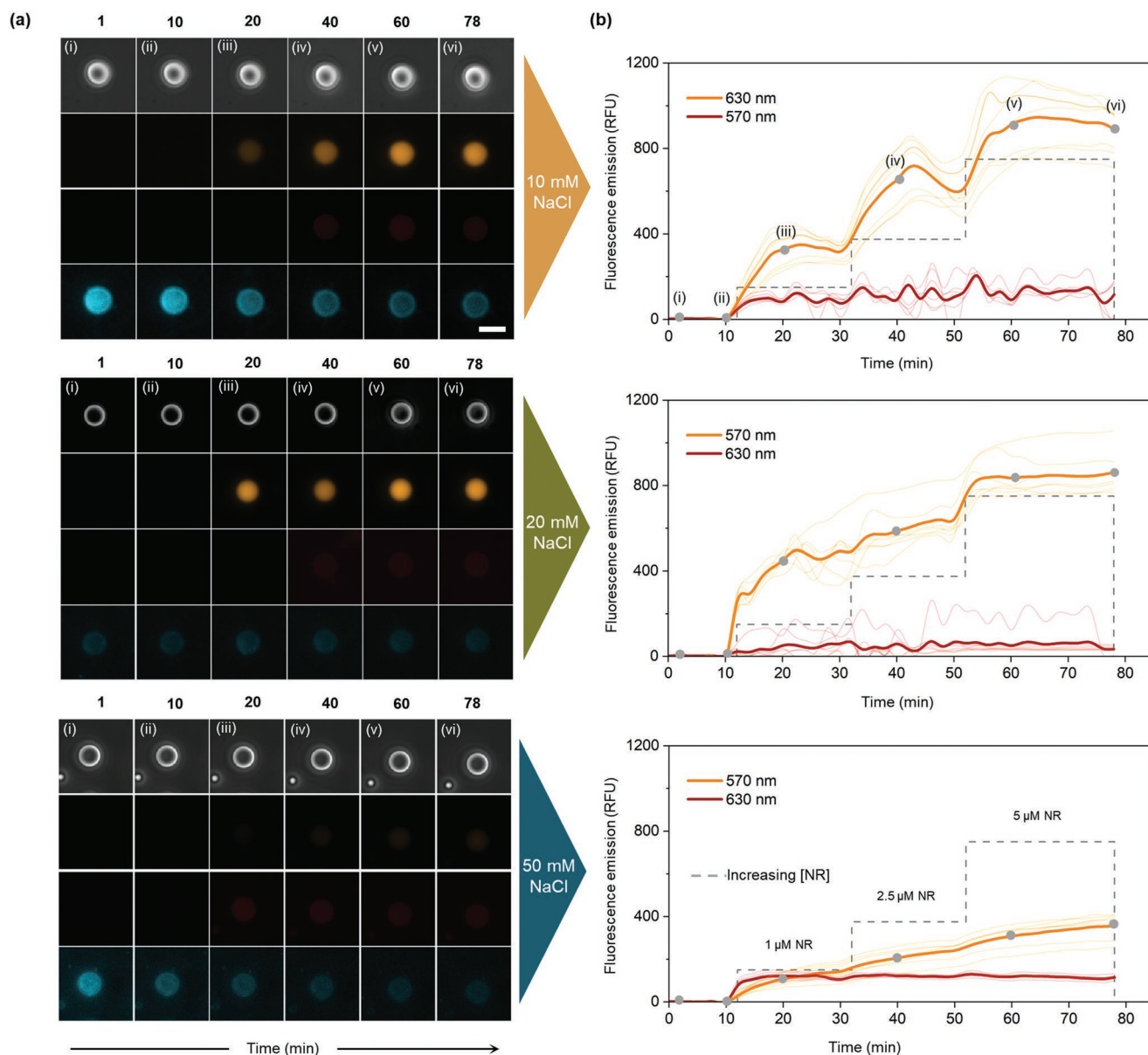


**Figure 6.** Time-resolved NR adsorption and permeation experiments with PE droplets ([NaCl]: 10, 20, or 50 mM) immobilized on poly-L-lysine coated glass slides and upon stepwise increasing the NR concentration from 1–5  $\mu\text{M}$ : a) microscopy contrast images (top) and fluorescent images acquired with the different filters for NR (570 and 630-nm channel, middle) and CFW (bottom) (20 $\times$  magnification, scale bar: 10  $\mu\text{m}$ ). The images were taken at different times during the NR-addition, corresponding to the points (gray circles) marked in (b). b) The development of the fluorescence intensities of the red (630 nm, o/w interface) and orange (570 nm, droplet core) channel, measured over the time, shows an early dye saturation at the interface, while NR continues to permeate into the droplet core for all salt concentrations at different permeation rates. The highlighted red/orange lines correspond to the average ( $n = 7$ ) of 7 individual droplets (faint lines), originating from three separate regions on the slide.

are closely related following the same trend that we observed before. Hence, CFW does not seem to influence the ratio between interface to droplet core fluorescence.

The micrographs in Figure 6a already show, for all three PEs, a relatively low interface NR fluorescence without any significant intensity increase with the increasing dye concentration. The oil-core fluorescence, in turn, visually increases throughout the feeding experiment, especially for the 10 and 20 mM NaCl PEs. The microscopy images also show the robustness of the PE droplets, which remain intact despite the significantly changing

surrounding conditions (e.g., excess of hydrophobic dye). The slight decrease in the cyan CFW fluorescence intensity arises from photobleaching effects due to the continuous exposure over the acquisition time, which we could also observe in a repeated exposure experiment (Figure S6, Supporting Information). Photobleaching affects all fluorescent dyes. However, the continuous/periodic addition of NR negates the observable photobleaching effects in the orange (570 nm) and red (630 nm) channels.

Figure 6b shows the development of the relative fluorescence emission intensity, acquired for the 630 nm and the 570 nm

channel over time and with respect to the injected NR concentration. It must be noted here that fluorescence intensity measurements are highly sensitive. Fluctuations in the single signals can, for example, already result from free droplets passing by the camera. Nevertheless, despite the observable fluctuations, the trend is very clear for each of the PEs.

For all [NaCl] studied, the o/w interface seems to saturate quickly already after injecting the 1  $\mu\text{M}$  NR solution, as indicated by the overall plateauing RFU for the 630 nm channel. The maximum interface fluorescence is relatively low (ca. 40–280 RFU) for all three PEs, which makes it difficult to observe any correlation with the salt content.

The droplet cores show a completely different development, with obvious differences for the three PEs. The 570 nm RFU intensity increases significantly with the increasing injected dye concentration. Particularly for the 10 and the 20 mM NaCl PE, the initial dye permeation into the droplets is very rapid after each new injection and plateaus or even starts to slightly decrease after about halfway in each NR cycle. This might indicate an equilibrium between dye incorporation and release adjusting itself while the dye concentration is kept constant, or slow photobleaching. Especially at high NR, the decrease in 570 nm signal could indicate droplet core saturation with dye and, consequently, fluorescence quenching.<sup>[45]</sup>

In contrast to the PEs prepared at 10 and 20 mM NaCl, the NR permeation into the 50 mM PE droplets followed an almost linear trend and a constant increase with the increasing dye concentration. A sign for droplet core saturation was not observed.

To provide quantitative analysis of the dye permeation into the different PE droplets, permeation rates were extracted, as a rough estimate, from linear fits (see Figure S7, Supporting Information) of the initial increase of the 570 nm fluorescence signal after each dye addition. Accordingly, the dye permeation rate into the 50 mM PE droplets was comparably slow (7–11 RFU/min) and steady without any significant increase for the higher dye concentrations. The 10 mM PE droplets gave a more than 4 times higher rate (ca. 38 RFU/min) in the RFU increase compared to the 50 mM PE. In the case of the 20 mM PE, the oil-core fluorescence level was comparable to the 10 mM PE droplets, but with relatively strong differences in the rate (11–49 RFU/min).

Overall, the time-resolved dye adsorption and permeation experiments support the trend we observed in this study: after rapid saturation of the o/w interface, NR continues to permeate into the oil droplet core. The rate of this permeation coincides with the salt concentration, which determines the density of the CNC layer at the o/w interface during the emulsion formation.

The lack of permeation into the droplet core at higher NaCl concentrations, for example, 50 mM, is related to non-specific interactions with the CNCs from the water and oil side. Consequently, densification of the CNC layer at the interface increases the accessible surface area for interactions with the dye molecules. Another key feature of our PE system is its remarkable robustness. What seems to matter for their stability are solely the conditions during the emulsion formation. The later change of the surrounding environment, as in our study (e.g., the excess of a hydrophobic dye, the presence of DMSO), did not affect the stability of the formed emulsion.

The permeability properties of the PE droplets motivated us to further explore their dynamic behavior and study the continuous filling and discharge of the droplet core. We used a comparable setup as with the time-resolved NR capture, with droplets immobilized on the microscopy slide. A 2.5  $\mu\text{M}$  concentration of NR was used to fill the droplet core. Each filling was followed by a wash with DI water to remove excess of dye from the liquid surrounding the droplets. After that, the droplet core was discharged/depleted using a 5% DMSO solution as a trigger (as illustrated in Figure 7a). These steps were repeated for 5 cycles.

We compared the 10 and 50 mM NaCl droplets and observed a strong core fluorescence (57 nm, orange channel) in the 10 mM droplets, which was mostly absent in the 50 mM droplet core (Figure 7b,c,e). As expected, the 10 mM core had about a three- to fourfold increased capacity/intensity. In both the 10 and 50 mM NaCl droplets, the discharge cycles in 5% DMSO emptied the droplet cores stepwise, with levels almost reaching that of the background, indicating efficient discharge of the whole core. The interface fluorescence (630 nm, red channel) also demonstrated differences between the 10 and 50 mM, especially at the start of the first cycle (Figure S8, Supporting Information). After the third cycle, the shell intensities levelled off to comparable levels. This might indicate for changes in the CNC-covered interfacial layer of the 10 mM PE droplets. Nevertheless, both the 10 and 50 mM NaCl PE droplets displayed remarkable stability throughout the dynamic cycling. No visual changes in the capacity of the droplet core could be observed, even after repeated filling and discharging cycles. Analysis of the amplitude also reveals solid durability (Figure 7d). Especially for the 10 mM NaCl PE droplets, the amplitude of the droplet core remains stable throughout the five cycles, filling and discharging to comparable levels, thus, rendering a proof-of-concept of the reusability of this material. With this, we demonstrate the effortless extraction of a captured compound from a liquid–liquid environment through change of the surrounding phase conditions—a remarkable feature rendering this simple, low-tech system a unique material platform for applications in membranes, as well as controlled compound release. Besides the simplicity of the system, its adaptability, for example, through changes of the CNC surface chemistry, provides seemingly unlimited possibilities for tuning PEs toward the captured or released compound. For future studies, it would be highly interesting to investigate the interplay between compounds of different chemical natures and the surface chemistry of the CNCs. Also other factors, like the polarity of the encapsulated oil phase, might significantly affect the performance of CNC-stabilized PEs in compound capture and release.

### 3. Conclusion

In this study, we demonstrated the exceptional properties of seemingly a very simple system: we controlled the formation of oil-in-water Pickering emulsions, stabilized by negatively charged ( $-\text{COO}^-$ ) cellulose nanocrystals, at a micrometer- (i.e., the droplet sizes) and nanometer-scale (the CNC interface assembly) by systematically adjusting the electrolyte content in the water phase.

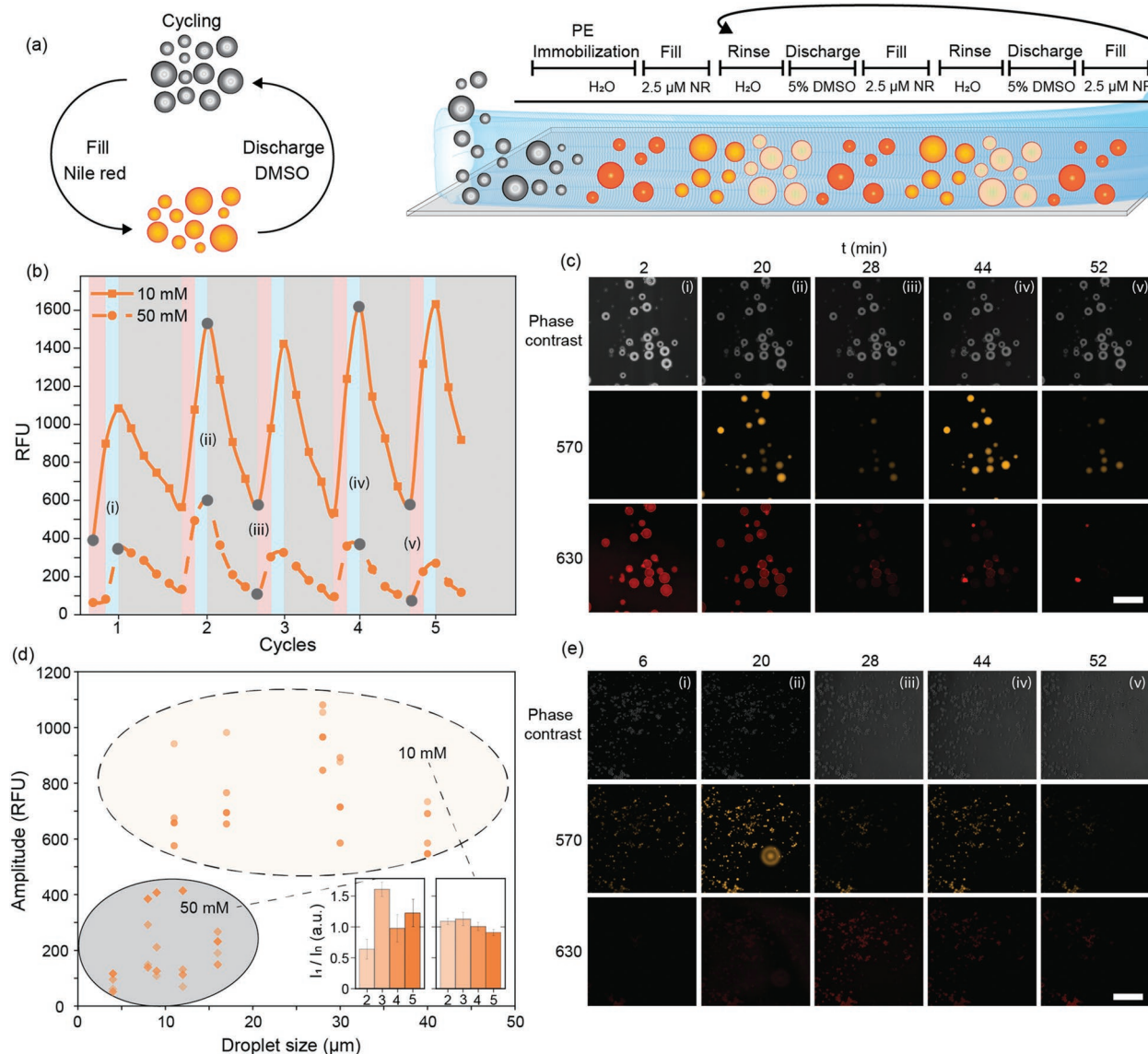


**Figure 7.** a) Schematic representation of time-resolved NR uptake and discharge experiments with PE droplets ([NaCl]: 10 or 50 mM) immobilized on poly-L-lysine coated glass slides. A total of 5 fill, rinse, and discharge cycles were studied. b) The development of the fluorescence intensities of the orange fluorescence (570 nm, droplet core) channel, measured over the time, reveals a clear larger capacity of the droplet core in 10 mM droplets. Background colors correspond to flow profiles, where red represents 2.5  $\mu\text{M}$  concentration of NR in 1% DMSO, blue represents DI water washes and grey a 5% DMSO cargo release trigger. c) Microscopy phase-contrast images (top) and fluorescent images acquired for NR (570 and 630-nm channel, middle and bottom) (20 $\times$  magnification, scale bar: 100  $\mu\text{m}$ ). Images were acquired at different times during the NR addition (gray circles in (b)). d) Comparison of the intensity difference for each cycle (amplitude, measured in RFU) between PE droplets ([NaCl]: 10 and 50 mM). Five individual droplets of varying sizes were analyzed per [NaCl] in 4 cycles. The 10 mM PE droplets have the capacity to fill and discharge to a far greater extent than 50 mM PE droplets, as seen in (c). Additionally, the amplitude (core intensity) is independent of droplet size (grey delineation ovals: 50 mM, beige: 10 mM) and demonstrates a remarkable stability and durability, especially of the 10 mM NaCl droplets. The zoom-in bar-graph displays the average scaled intensity ( $I_1/I_{(n+1)}$  [a.u.]) of all measured droplet amplitudes, where each cycle ( $I_2$ ,  $I_3$ ,  $I_4$ , and  $I_5$ ) is compared to the first amplitude ( $I_1$ ) of each individual droplet. e) Fluorescent intensities as described in (c) for 50 mM NaCl PE droplets (20 $\times$  magnification, scale bar: 100  $\mu\text{m}$ ).

The addition of NaCl led to a stabilization of the biphasic system already at low salt concentrations (10 mM), and to decreasing droplet sizes with the increasing [NaCl]. The o/w interface permeability, probed with the solvatochromic dye Nile red and a combined setup of fluorescence spectroscopy and microscopy, was determined by the salt concentration used during the emulsion preparation. The increasing electrolyte

content (between 10–100 mM NaCl) thereby coincided with a densification of the layer of the anionic CNCs at the o/w interface, which was characterized by a slower permeation of the dye into the droplets. This behavior was very uniform for the PE droplets and independent of their actual size, removing the need for complicated purification/separation steps. Last, we demonstrated the applicability of this system

in sustainable technologies such as water remediation, due to the reusability of the system demonstrated in the cyclic uptake–release of organic pollutants in aqueous media.

Our setup of fluorescence experiments, using a hydrophobic, solvatochromic probe, has served as an indirect tool to visualize the properties of the CNC layer at the o/w interface. This significantly contributes to understanding and exploiting the controllability of nanocellulose-stabilized emulsions, for which the electrolyte content, in the interplay with the CNC surface charge, is an important design parameter. Understanding will ultimately lead to practical applications of PEs, in which the attractiveness of the system clearly lies in its versatility, simplicity and scalability opening-up a cost-effective, low-tech avenue toward well-defined, functional materials ranging from smart membranes to controlled-release systems. The concomitancy of this cheap and simple synthetic approach with the high performance based in robustness and reusability renders a unique material with direct application in clean water technologies affordable in developing countries.

#### 4. Experimental Section

**Materials:** Commercial bacterial cellulose (Nata-de-Coco) was purchased from an ethnical grocery store in Helsinki, Finland, and purified according to the procedures described in the Supporting Information. HCl gas (99.8%, 10 dm<sup>3</sup>, 6 kg) was purchased from AGA (Sweden). 50% aqueous NaOH, which was diluted and used to neutralize acid gas residues, was purchased from AKA Chemicals, Finland. 2,2,6,6-tetramethyl-1-piperidinyloxy (TEMPO, free radical, 98%), n-dodecane (≥99.0%), sodium chloride (ACS reagent, ≥99.0%), 1 M NaOH (Merck [Darmstadt, Germany]), 1 M HCl (Merck [Darmstadt, Germany]), sulfuric acid (95–97%, EMSURE), poly(ethylenimine) ( $M_w \approx 2000$  [LS], 50% in water), 0.01% poly-L-lysine (w/v in DI water), Nile red and calcofluor white (for microscopy) were all purchased from Sigma Aldrich (Finland). Dialysis membranes (Spectra/Por 1, MWCO 6–8 kDa), 13% NaOCl and 3.5% NaOCl solution were received from VWR (Finland). Millipore-processed deionized (DI) water (resistivity of 18.2 MΩ cm) was used for all experiments.

**Preparation of TEMPO-CNCs from Bacterial Cellulose:** Detailed protocols for the TEMPO-CNC preparation and characterization can be found in Sections S1 and S2, Supporting Information. Surface-oxidized CNCs were prepared from commercial bacterial cellulose (BC) by a combined HCl-gas hydrolysis and TEMPO-oxidation as described earlier.<sup>[41,48]</sup> Disintegration and dispersion of the hydrolyzed and oxidized BC gel was achieved by a high-pressure microfluidization (Microfluidics M110P) fluidizer, 200/400 μm chamber pair, and constant pressure of 1500 bar (Section S1d, Supporting Information). The degree of polymerization (DP) of the hydrolyzed BC was determined directly after hydrolysis by viscometry (CED-viscosity, Section S2a, Supporting Information).<sup>[49]</sup> The surface charge of the hydrolyzed and oxidized material was determined by conductometric titration (Section S2b, Supporting Information). Before further analysis and emulsion preparation, the pH of the CNC dispersion was adjusted to 7.5 with 0.1 M NaOH and the TEMPO-CNCs were purified by dialysis (Spectra/Por 1, MWCO 6–8 kD) against DI water until a conductivity of <5 μS was reached. After the purification, the CNCs were imaged by atomic force microscopy (AFM) for dimensional characterization<sup>[50]</sup> (Section S2c, Supporting Information) and their zeta potential (Section S2d, Supporting Information) was determined.

**Preparation of Nanocellulose-Stabilized Pickering Emulsions:** For each salt condition, 6 mL o/w PEs were prepared at a constant dodecane-to-water ratio of 40:60 (v/v) in 20-mL snap-cap glass vials. Before the emulsification, the CNC concentration in the water phase (total volume 3.6 mL) was adjusted to 0.50 wt% with water or aqueous NaCl

solution reaching final salt concentrations of 0, 10, 20, 50, or 100 mM. The dispersions were thoroughly mixed before adding the oil. Then, 2.4 mL dodecane was added and the two phases were blended first on a vortex shaker (IKA Vortex 3, level 4) for 30 s and immediately afterward emulsified with a homogenizer (T10 basic Ultra-Turrax, IKA) at 30 000 rpm for 3 min, using an IKA S 10 N – 10 G disperser tool (1–100 mL). To avoid overheating during the emulsification, the emulsions were constantly cooled in an ice bath. After the emulsification, the freshly prepared and still homogeneous PEs were immediately aliquoted for the different measurements. All characterizations (e.g., droplet size measurements, fluorescence spectroscopy) were conducted the day after the emulsion preparation ensuring an equilibration of the system.

**Optical Microscopy:** Optical micrographs were acquired from diluted PEs (1:2 [v/v] with DI water or NaCl solution [10, 20, 50, or 100 mM]) on standard glass microscopy slides with a Leica DMIL LED microscope, equipped with a Leica DFC3000 G camera. Images were recorded and analyzed with the software Leica Application Suite X (version 3.6.1.23246).

**Droplet Size Measurements by Laser-Light Diffraction (LLD):** Droplet size distributions were determined by laser-light diffraction (LLD) on a Malvern Mastersizer 2000 (Malvern Panalytical Ltd, Malvern, UK) in a size range of 0.2–2000 μm. DI water ( $n_D = 1.33$ , 25 °C) served as a dispersant to which the PE droplets were added directly. Dodecane was selected as dispersed phase ( $n_D = 1.421$ , 25 °C). For each salt condition, two PEs were prepared and analyzed. Average values for the median particle size ( $d_{50}$ ),  $d_{90}$  (90% of droplets < given size), and  $d_{10}$  (10% of droplets < given size) were calculated automatically from triplicate measurements by the instrument's software, from a preadjusted measurement time of 5 s and 5000 accumulated points (for background and samples).

**Fluorescence Spectroscopy:** The optical properties and solvatochromic effect of Nile red (NR) in the presence of PEs and suitable controls were characterized by fluorescence spectroscopy, using a Cytation 3 plate reader (BioTek, Winooski, VT, USA) with an excitation at  $\lambda_{exc} = 535$  nm, and an emission between  $\lambda_{em} = 562$ –700 nm. The gain was set to 75%, and the reading height to 7 mm from the bottom of the plate. The samples were initially prepared using 500 μL Eppendorf tubes and then transferred to a clear flat-bottom 96-well plate (Corning) for the measurements. A detailed description of the sample preparation (PEs and controls) can be found in Section S4, Supporting Information. Initial spectral measurements were carried out at a low NR charge with each of the prepared PEs (0–100 mM NaCl). The samples were equilibrated for at least 1 h with 1 vol% of a 5 μM NR solution in DMSO, corresponding to a final dye concentration in the PEs of 50 nM. The DMSO content of 1 vol% in the emulsions ensured the solubility NR in the samples. Spectral acquisition and endpoint analysis at 570 and 630 nm were carried out in triplicate samples. In the second part of the experiment, spectral acquisition and endpoint analysis were repeated with three selected PEs (10, 20, and 50 mM NaCl) which were equilibrated with a high NR charge of 5 μM. The dye concentration was kept constant, while the PEs were diluted to investigate how different emulsion systems behave when increasing the NR to CNC ratio (see Tables S2 and S3, Supporting Information) above the aqueous solubility limit of NR.

**Fluorescence Microscopy:** For the immobilization of the emulsion droplets, microscopy slides (26 × 76 mm cover glasses, Menzel Gläser, Thermo Fisher Scientific) were coated similarly to the Si-wafers used for atomic force microscopy (AFM) analysis with the positively charged polymer poly(ethyleneimine) (PEI) (see Sections S2c and S5a, Supporting Information). The PEs with [NaCl] 0–100 mM were equilibrated for at least 1 h with 1 vol% of a 1 mM NR DMSO solution, reaching a final NR concentration of 10 μmol L<sup>-1</sup>. The equilibrated PEs were placed directly on the PEI coated slides, followed by washing with DI water to remove unbound emulsion droplets. For the 100× magnification analysis and 3D reconstructions, this was followed by a wash with a Calcofluor white stain (1:1 Calcofluor white 55 μM in water and 10% aqueous KOH), for 1 min. This was followed by several washing steps with DI water to remove unbound stain. The immobilized

droplets were covered immediately with a water layer and a small cover slide to prevent them from drying.

Both phase contrast and fluorescence microscopy images were acquired with an Axio Observer Z1 microscope (Carl Zeiss, Jena, Germany), equipped with an iXon Ultra 888 EMCCD camera (Andor Technology, Belfast, United Kingdom) and automated stage. Images were captured with a 10 × 0.3 Ph1 objective, a 20 × 0.6 Khor Ph2 objective and a 40 × 0.6 Khor Ph2 objective, combined with a 1.6 optovar. The cyan fluorescence signal (Calcofluor white) was collected using a 420 nm illumination with 418–442 nm excitation filter and 461–485 emission. For the Nile red emission, the orange fluorescence signal was collected using 530 nm illumination with 528–550 nm emission filter and 560–584 emission. The red fluorescent signal was collected using 530 nm illumination with 528–550 nm emission filter and 615–675 emission. For the profile analysis, the fluorescence intensity at each of the different channels was acquired over the whole area of 50 selected droplets (size range: 3–55 μm in diameter) using the Zen-Blue software.

**Time-Resolved Nile Red Uptake:** Time-resolved experiments were carried out by fluorescence microscopy. For the immobilization of the emulsion droplets, microscopy slides were coated with filter-sterilized 0.01% poly-L-lysine (w/v in DI water) for 1 h prior to immobilization of the PE droplets, providing stronger interactions between the surface and the PE droplets in comparison to PEI. The glass slides were then washed repeatedly with DI water, after which the solution of PE droplets was applied on the glass slide for ≈5 min (during which the droplets were rehydrated when needed, to prevent drying). This was followed by repeatedly rinsing with DI water to remove unbound droplets, after which the bound droplets were coated with CFW (as described in fluorescence microscopy section) and repeatedly rinsed again with DI water. The slide was then mounted in the microscope frame, and a minimum of three different regions (tiles) were identified and selected for continuous acquisition. After the start of the acquisition, three different concentrations of Nile red (1, 2.5 and 5 μM), dissolved in a 1 vol% DMSO solution in water, were sequentially pipetted into the water-submerged droplets in a 100 μL volume at 12, 34 and 56 min, respectively. Equal volumes (100 μL) were pipetted out of the solution from the opposite end of the submerged droplets, to keep the volume equal. Images were acquired every 2 min from 7 individual droplets, located on 3 different regions, to ensure that the observations were uniformly represented in the particles on the slide. Definite focus was used prior to each acquisition event, to ensure the correct focus of the PE droplets.

**Time-Resolved Nile Red Uptake and Discharge Cycles:** Glass slides with PE droplets of both 10 and 50 μm were prepared as described in Time-resolved Nile red capture. The slide was then mounted in the microscope frame and rehydrated with DI water. Phase contrast and 570 and 630 nm fluorescent images were acquired every 2 min. After the start of acquisition, 2.5 μM concentration of Nile Red was used to fill the droplets for 2 min. This was followed by a rinse to remove excess and unbound Nile red, with DI water for 2 min. The rinse was followed by 8 min with 5% DMSO to deplete the droplet core. After depletion, PE droplets were filled again with 2.5 μM for 2 min. The fill, rinse, and discharge cycle was repeated for 5 times.

**Statistical Analysis:** Sample sizes ( $n = *$ ) for each figure and statistical analysis (mean ± SD), where appropriate, are included in the figure legends. Image processing is further discussed in the Fluorescence Microscopy section of the Experimental Section. No other statistical methods were applied in this work.

## Supporting Information

Supporting Information is available from the Wiley Online Library or from the author.

## Acknowledgements

K.H. and C.J. contributed equally to this work. K.H. gratefully acknowledges the postdoctoral grant received from the Academy

of Finland (grant number: 333905). The authors would also like to acknowledge the Academy of Finland Centre of Excellence in Life-Inspired Hybrid materials (LIBER 346105).

## Conflict of Interest

The authors declare no conflict of interest.

## Data Availability Statement

The data that support the findings of this study are available from the corresponding author upon reasonable request.

## Keywords

colloidal assembly, controllable template, liquid interfaces, nanomaterials

Received: April 28, 2022

Revised: June 15, 2022

Published online: August 19, 2022

- [1] D. Suzuki, S. Tsuji, H. Kawaguchi, *J. Am. Chem. Soc.* **2007**, *129*, 8088.
- [2] B. Liu, W. Wei, X. Qu, Z. Yang, *Angew. Chem.* **2008**, *120*, 4037.
- [3] Z. Rozynek, A. Mikkelsen, P. Dommersnes, J. O. Fossum, *Nat. Commun.* **2014**, *5*, 3945.
- [4] H. Yang, L. Fu, L. Wei, J. Liang, B. P. Binks, *J. Am. Chem. Soc.* **2015**, *137*, 1362.
- [5] N. Xue, G. Zhang, X. Zhang, H. Yang, *Chem. Commun.* **2018**, *54*, 13014.
- [6] W.-L. Jiang, Q.-J. Fu, B.-J. Yao, L.-G. Ding, C.-X. Liu, Y.-B. Dong, *ACS Appl. Mater. Interfaces* **2017**, *9*, 36438.
- [7] Z. Sun, U. Glebe, H. Charan, A. Böker, C. Wu, *Angew. Chem.* **2018**, *130*, 14006.
- [8] A. Moreno, M. H. Sipponen, *Nat. Commun.* **2020**, *11*, 5599.
- [9] M. Destribats, B. Faure, M. Birot, O. Babot, V. Schmitt, R. Backov, *Adv. Funct. Mater.* **2012**, *22*, 2642.
- [10] Y. Li, X. Liu, Z. Zhang, S. Zhao, G. Tian, J. Zheng, D. Wang, S. Shi, T. P. Russell, *Angew. Chem., Int. Ed.* **2018**, *57*, 13560.
- [11] Z. Zhao, Y. Liu, K. Zhang, S. Zhuo, R. Fang, J. Zhang, L. Jiang, M. Liu, *Angew. Chem.* **2017**, *129*, 13649.
- [12] Y. Bai, C. Wang, F. Zhang, J. Tan, K. Xu, Y. Tan, P. Wang, *Polymer* **2020**, *186*, 122057.
- [13] J. Wu, G.-H. Ma, *Small* **2016**, *12*, 4633.
- [14] J. Tang, P. J. Quinlan, K. C. Tam, *Soft Matter* **2015**, *11*, 3512.
- [15] H. Jiang, Y. Sheng, T. Ngai, *Curr. Opin. Colloid Interface Sci.* **2020**, *49*, 1.
- [16] N. Scheuble, J. Schaffner, M. Schumacher, E. J. Windhab, D. Liu, H. Parker, A. Steingoetter, P. Fischer, *ACS Appl. Mater. Interfaces* **2018**, *10*, 17571.
- [17] Y. Zhu, W. Wang, H. Yu, A. Wang, *J. Environ. Sci.* **2020**, *88*, 217.
- [18] M. A. Hussein, A. A. Mohammed, M. A. Atiya, *Environ. Sci. Pollut. Res.* **2019**, *26*, 36184.
- [19] M. Sjöö, S. C. Emek, T. Hall, M. Rayner, M. Wahlgren, *J. Colloid Interface Sci.* **2015**, *450*, 182.
- [20] I. Kalashnikova, H. Bizot, P. Bertoncini, B. Cathala, I. Capron, *Soft Matter* **2013**, *9*, 952.
- [21] A. Mautner, *Polym. Int.* **2020**, *69*, 741.

- [22] F. Sicard, J. Toro-Mendoza, *ACS Nano* **2021**, *15*, 11406.
- [23] I. Capron, O. J. Rojas, R. Bordes, *Curr. Opin. Colloid Interface Sci.* **2017**, *29*, 83.
- [24] L. Bai, L. G. Greca, W. Xiang, J. Lehtonen, S. Huan, R. W. N. Nugroho, B. L. Tardy, O. J. Rojas, *Langmuir* **2019**, *35*, 571.
- [25] P. Bertsch, P. Fischer, *Adv. Colloid Interface Sci.* **2020**, *276*, 102089.
- [26] G. Dockx, S. Geisel, D. G. Moore, E. Koos, A. R. Studart, J. Vermant, *Nat. Commun.* **2018**, *9*, 4763.
- [27] B. Pang, H. Liu, K. Zhang, *Adv. Colloid Interface Sci.* **2021**, *296*, 102522.
- [28] N. Ghavidel, P. Fatehi, *ChemSusChem* **2021**, *14*, 4850.
- [29] K. Heise, E. Kontturi, Y. Allahverdiyeva, T. Tammelin, M. B. Linder, Nonappa, O. Ikkala, *Adv. Mater.* **2021**, *33*, 2004349.
- [30] F. Cherhal, F. Cousin, I. Capron, *Biomacromolecules* **2016**, *17*, 496.
- [31] W. Du, J. Guo, H. Li, Y. Gao, *ACS Sustainable Chem. Eng.* **2017**, *5*, 7514.
- [32] Z. Zhang, K. C. Tam, X. Wang, G. Sèbe, *ACS Sustainable Chem. Eng.* **2018**, *6*, 2583.
- [33] A. G. Cunha, J.-B. Mougèl, B. Cathala, L. A. Berglund, I. Capron, *Langmuir* **2014**, *30*, 9327.
- [34] I. Kalashnikova, H. Bizot, B. Cathala, I. Capron, *Biomacromolecules* **2012**, *13*, 267.
- [35] P. Bertsch, M. Diener, J. Adamcik, N. Scheuble, T. Geue, R. Mezzenga, P. Fischer, *Langmuir* **2018**, *34*, 15195.
- [36] J. Bergfreund, Q. Sun, P. Fischer, P. Bertsch, *Nanoscale Adv.* **2019**, *1*, 4308.
- [37] S. Varanasi, L. Henzel, L. Mendoza, R. Prathapan, W. Batchelor, R. Tabor, G. Garnier, *Front. Chem.* **2018**, *6*, 409.
- [38] V. Calabrese, J. C. Courtenay, K. J. Edler, J. L. Scott, *Curr. Opin. Green Sustainable Chem.* **2018**, *12*, 83.
- [39] F. Cherhal, F. Cousin, I. Capron, *Langmuir* **2015**, *31*, 5596.
- [40] P. Bertsch, S. Isabettoni, P. Fischer, *Biomacromolecules* **2017**, *18*, 4060.
- [41] T. Pääkkönen, P. Spiliopoulos, Nonappa, K. S. Kontturi, P. Penttilä, M. Viljanen, K. Svedström, E. Kontturi, *ACS Sustainable Chem. Eng.* **2019**, *7*, 14384.
- [42] M. M. Robins, *Curr. Opin. Colloid Interface Sci.* **2000**, *5*, 265.
- [43] L. Liu, Z. Hu, X. Sui, J. Guo, E. D. Cranston, Z. Mao, *Ind. Eng. Chem. Res.* **2018**, *57*, 7169.
- [44] P. K. Weissenborn, R. J. Pugh, *J. Colloid Interface Sci.* **1996**, *184*, 550.
- [45] T. G. W. Edwardson, S. Tetter, D. Hilvert, *Nat. Commun.* **2020**, *11*, 5410.
- [46] G. Hungerford, E. M. S. Castanheira, M. E. C. D. R. Oliveira, M. da Graça Miguel, H. D. Burrows, *J. Phys. Chem. B* **2002**, *106*, 4061.
- [47] J. Plášek, B. Hošková, *J. Fluoresc.* **2010**, *20*, 343.
- [48] T. Pääkkönen, C. Bertinetto, R. Pönni, G. K. Tummala, M. Nuopponen, T. Vuorinen, *Appl. Catal., A* **2015**, *505*, 532.
- [49] M. Marx-Figini, *Angew. Makromol. Chem.* **1978**, *72*, 161.
- [50] C. A. Schneider, W. S. Rasband, K. W. Eliceiri, *Nat. Methods* **2012**, *9*, 671.